Mechanics Research Communications 150 (2025) 104555

Contents lists available at ScienceDirect

Mechanics Research Communications

journal homepage: www.elsevier.com/locate/mechrescom

Detachment stability maps of bi-material composite fibrils

András Levente Horváth, Attila Kossa *

Budapest University of Technology and Economics, Faculty of Mechanical Engineering, Department of Applied Mechanics, Műegyetem rkp. 3, Budapest, H-1111, Hungary

ARTICLE INFO

Keywords:
Composite fibril
Adhesion
Stability
Energy release rate
Finite element analysis
Bi-material

ABSTRACT

In this study, we examine the detachment stability behavior of axisymmetric bi-material composite fibrils. Our goal is to determine the stable and unstable detachment domains as a function of different geometric and material parameters, such as layer thickness or the elastic modulus ratio. The numerical results are obtained using finite element simulations. Two cases are investigated: edge detachment and center detachment. We use the derivative of the energy release rate with respect to the contact surface area to determine the stability behavior. In our parametric study, we vary the dimensionless thickness of the soft tip layer, the ratio of the elastic moduli of the materials, and the Poisson's ratio. The stability maps shown in the paper are based on the evaluation of more than half a million finite element simulations. Our results show that for both types of detachment, there exists a critical layer thickness above which only unstable detachment can develop. We also show that increasing the ratio of the elastic moduli increases the size of the stable region, but there is a lower limit below which no stable detachment is observed, regardless of the size of the defect. Reducing the Poisson's ratio decreases the size of the stable region but has little effect on its overall shape. These new results contribute to a better understanding of the detachment mechanisms in composite fibrillar adhesive systems and provide a basis for further research on other material pairings and geometric configurations.

1. Introduction

The study of adhesion phenomena remains highly important today, as researchers aim to develop increasingly advanced engineering applications where the connection between bodies is realized through adhesion, making use of the advantages of adhesive bonding [1,2]. The development of these applications includes the use of modern new base materials, the application of more precise manufacturing methods, and accurate mechanical modeling. One of the most well-known engineering applications of dry adhesive bonding is the use of gecko-inspired fibrillar structures to grip and move objects [3,4]. Several scientific articles present different designs of fibrillar structures for such purposes. One of the design goals during the development of such fibrillar structures is to ensure that the resulting adhesive connection is as strong and as resistant to loading as possible. The nature of the stress distribution along the contact surface has a direct effect on the adhesive connection, especially when we consider that small irregularities may be present between the surfaces during attachment, which can cause local stress concentration. For this reason, a possible design approach is to reduce stress magnitude at critical locations, which in the case of a cylindrical fibril typically appear along the perimeter, where we may assume that a perfect contact has not formed between the surfaces. In these singularity regions, mechanical stresses can be reduced either by a suitable modification of the geometry or by changing the material properties. An example of the former is the application of a mushroom-shaped fibril, while an example of the latter is the use of a bi-material composite fibril or a fibril with a non-homogeneous elastic modulus [5–8].

A large number of studies have focused on the mechanics and adhesion performance of mushroom-shaped fibrils, addressing several additional modeling aspects such as the origin of their superior adhesive performance, the role of viscoelasticity, the dynamic adhesion behavior of micropillars, and the fabrication of mushroom-shaped adhesive structures with smooth contours via electrical growth [9–12].

In addition to understanding the stress distribution, it is especially important to study the nature of the separation process during the detachment of the adhesive connection. Is it necessary to invest additional energy to initiate the separation of the surfaces, or does the behavior of the system ensure that the surfaces separate without the need for additional external work? In this sense, we can speak about the stability of surface detachment, which is less frequently addressed in detail in scientific articles, although its understanding is particularly important from an application point of view.

A key study in the investigation of detachment stability is the 2003 work by Webber and co-authors, in which they show the critical

* Corresponding author.
E-mail address: kossa@mm.bme.hu (A. Kossa).

https://doi.org/10.1016/j.mechrescom.2025.104555
Received 30 July 2025; Received in revised form 12 October 2025; Accepted 25 October 2025
Available online 30 October 2025

layer thickness above which stable detachment can no longer occur in the case of a rigid cylindrical punch adhered to an infinite elastic layer [13,14]. The examination of this phenomenon requires the analysis of the energy release rate, a concept introduced in classical fracture mechanics. The methodology presented in that paper can also be applied to structures with different geometries and material compositions. A recent study describes in detail the critical chip thickness values in the poker chip problem above which stable detachment cannot develop [15]. The aforementioned study presents both edge and center detachment cases, and it specifically analyzes the effect of the Poisson's ratio on the stability boundaries. The generation of the stability maps shown in the mentioned paper required a large number of finite element simulations, considering that the studied problem has no analytical solution.

The aim of the present study is to investigate the bi-material composite fibril in detail from the viewpoint of detachment stability in adhesive contacts. In the case of a bi-material composite fibril, a cylindrical punch is connected to a rigid substrate. At the end of the cylindrical punch, a soft tip made of a more compliant material is attached, which helps to reduce stress values at the perimeter, thereby increasing the resistance of the adhesive connection in the presence of edge defects. Using a suitable finite element model, we determine the strain energy values for different geometries and material compositions of composite fibrils for both edge and center detachment cases. A sufficiently fine resolution is applied to the initial defect sizes in both detachment modes, allowing the energy release rate to be determined accurately. From the high-resolution results of the energy release rate, we generate stability maps and show how detachment stability changes as a function of soft tip thickness and the ratio of elastic moduli. In addition, we also examine the effect of Poisson's ratio on the stability maps.

The fabrication of bi-material fibrils with distinct mechanical properties is technically feasible, and several studies have demonstrated their experimental realization. For example, two-step moulding processes allow polymer layers with different elastic moduli to be combined into a single composite structure [5]. Similar manufacturing approaches can be implemented using materials such as PDMS, polyurethane, or epoxy, where tuning the degree of crosslinking or the filler content can lead to significant differences in stiffness. The Poisson's ratio can also be adjusted, although within a narrower range, by modifying the microstructure or porosity of the material. Rather than reproducing a specific material combination, the present work aims to explore a wide range of geometric and material configurations to support future experimental design and material optimization.

In the Section 2 of the paper, we present the mechanical problem to be solved and the methodology used for the stability analysis. In the Section 3, we describe the finite element model used for the simulations and the calculation procedure of the energy release rate. In the Section 4, we present the computed stability maps for both cases (edge and center detachment) for various Poisson's ratios and elastic modulus ratios, and provide both qualitative and quantitative analysis based on these results. The Section 5 provides additional discussion and remarks. The Section 6 summarizes the main conclusions of the study. Finally, the Appendix presents the details of the mesh layout and the results of the mesh convergence analysis.

2. Problem description

The composite fibril is modeled as a cylindrical body made of two elastic materials. The fibril adheres to a rigid substrate through an adhesive connection. Under tensile loading, detachment can occur at the contact surface if a critical load is reached. In practical cases, detachment usually develops near imperfections in the adhesive contact. Nevertheless, it should be noted that other types of failure may also occur, for example when internal voids form in the elastic material under sufficiently high tensile loads [16]. This phenomenon has been discussed in several scientific papers, but the present work does not investigate this case. Instead, we focus on detachment that develops along the contact surface, which is governed by different mechanisms. It should also be noted that in the case of pure dry adhesion, the adhesive bond usually fails before voids can form in the material.

To investigate the stability of the adhesive connection along the contact surface, we employ the classical theory of fracture mechanics, as many other researchers also use this approach when studying similar phenomena [17,18]. The detachment is modeled as a crack propagating between the rigid substrate and the elastic body. It should be noted that in reality the substrate is not perfectly rigid, but since its elastic modulus is orders of magnitude higher than that of the elastic fibril, it is a reasonable approximation for the analysis to assume the substrate to be ideally rigid. The concept of energy release rate is applied to study detachment stability [19]. The energy release rate (G) is defined as the decrease of potential energy (π) per unit decrease of contact area (A):

$$G = \frac{\partial \pi}{\partial A}. \tag{1}$$

Detachment propagation initiates once a critical value of G is reached, which depends on the strength of the adhesive bond. The stability of the propagation indicates whether external energy is required for continued propagation. Stable detachment requires additional external work to propagate, while unstable propagation does not, as the decrease of potential energy covers the energetic cost of creating the new surface. Stability can be assessed through the partial derivative of the energy release rate. Importantly, detachment stability does not depend on the type and strength of adhesion between the elastic body and the rigid plate. We investigate a displacement-driven case; thus, the potential energy (π) is equal to the stored strain energy in the system (U). For this reason, it is sufficient to analyze the strain energy for all of our calculations. The condition for stable detachment propagation in the displacement-driven case is formulated as

$$0 < \frac{\partial G}{\partial A} = \frac{\partial^2 \pi}{\partial A^2} = \frac{\partial^2 U}{\partial A^2}. \tag{2}$$

The bi-material composite fibril model is an important extension of the poker-chip model, which was analyzed in previous studies, including earlier work by the authors [15,20]. In the case of a bi-material composite fibril, we represent the elastic fiber with two elastic layers: the upper layer models the stiffer stalk, while the lower layer represents the soft fibril tip, as illustrated in Fig. 1. Each layer has homogeneous material properties. We consider two axisymmetric detachment modes that initiate at the bottom interface. These initiate from either the edge or the center of the circular fibril and are therefore referred to as edge and center detachment, respectively. These detachment modes are schematically illustrated in Fig. 2.

Despite the simple geometry, there is no closed-form analytical solution for the stress distribution along the interface; only asymptotic and approximate solutions exist [21]. Likewise, no analytical expression is available for calculating the strain energy of the system, and therefore stability cannot be evaluated using purely analytical methods.

We investigate this problem using numerical tools, particularly the finite element method (FEM). This approach allows us to explore a wide range of model parameters and analyze quantities that are difficult to measure experimentally. FEM is well suited for determining the stored strain energy (U) in the system, which is essential for the stability calculations.

Consequently, the main task is to calculate the strain energy for the bi-material composite fibril shown in Fig. 1, considering different layer thicknesses and elastic modulus ratios for both edge and center detachment cases, each with various initial defect sizes.

3. Numerical model

In the investigated problem, Hooke's law is used to describe the material behavior, assuming small strains and deformations, since large

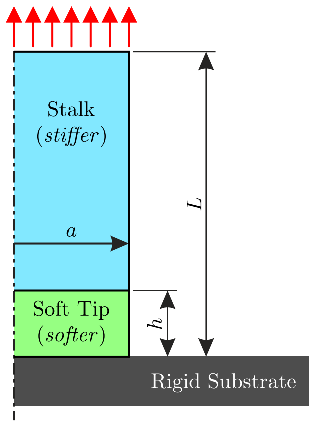

Fig. 1. Schematic axisymmetric model of the bi-material composite fibril used in the study. The fibril consists of a stiff stalk and a soft tip, with total length L, radius a, and soft tip thickness h. The initial detachment length is not indicated in the figure.

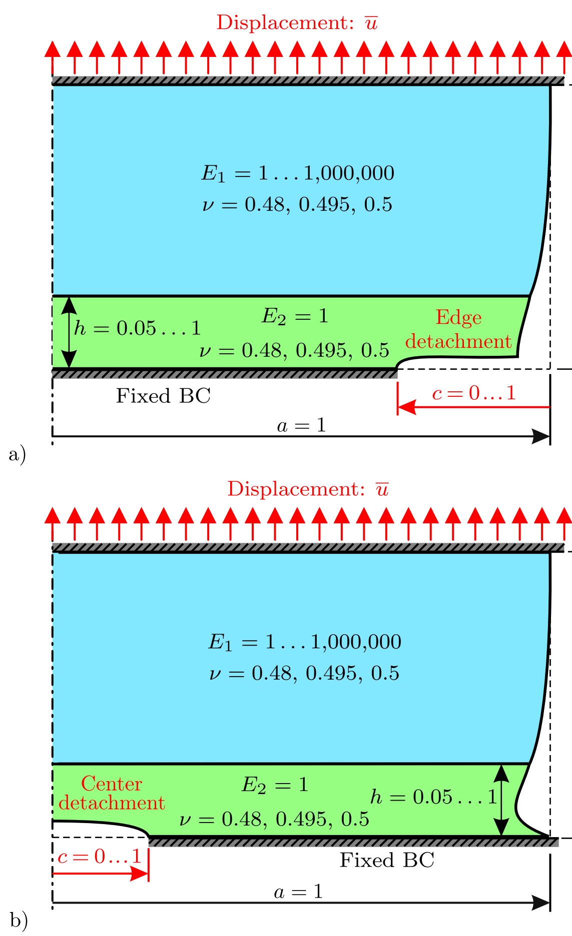

Fig. 2. Schematic illustration of the investigated detachment modes in their deformed configurations: (a) edge detachment and (b) center detachment. The displacements are exaggerated for clarity to highlight the detachment process. Key geometric parameters and boundary conditions used in the numerical simulations are also indicated in the figures.

deformations are not expected. In real situations, the adhesive bond typically fails before the system reaches the large-deformation range; therefore, geometric nonlinearity does not need to be considered. In our calculations, we examine the influence of three main parameters: the layer thickness of the soft tip, the ratio of the elastic moduli, and the value of the Poisson's ratio.

Table 1
Summary of the parameter ranges considered in the numerical simulations, including detachment type, modulus ratio, soft layer thickness, Poisson's ratio, and detachment length. These parameters define the scope of the parametric study presented in this work.

Parameter	Value
Detachment type	Edge or center
Modulus ratio (E_1/E_2)	1 …1,000,000
Soft layer thickness (h/a)	0.05…1.0
Poisson's ratio (ν)	0.48, 0.495, 0.5
Detachment length (c/a)	0.004 …0.996

Artificial structures with dry adhesive properties are usually made from polymer-like materials that are nearly incompressible; thus, $\nu \approx 0.5$ is a reasonable assumption. However, even small deviations from perfect incompressibility can noticeably affect the stability properties [15]. For this reason, we consider multiple values of ν. The value $\nu = 0.5$ corresponds to volumetric incompressibility, $\nu = 0.495$ represents a typical measured value for manufactured dry adhesive structures [22], and $\nu = 0.48$ is selected as the lowest value in this study to investigate the influence of volumetric compressibility. In the present work, both the stiffer stalk and the soft tip are assumed to share the same Poisson's ratio.

The materials are further characterized by the elastic moduli of the top (E_1) and bottom (E_2) layers. Only the ratio of these quantities affects the stability properties; therefore, E_2 is set to $E_2 = 1$ MPa. The system is characterized by the modulus ratio E_1/E_2, which is one of the key parameters in this work. The ratio E_1/E_2 is varied between $E_1/E_2 = 1$ (representing a homogeneous material) and $E_1/E_2 = 1{,}000{,}000$ (representing a rigid stalk). In total, 13 different values were analyzed for edge detachment and 16 for center detachment.

Geometry is characterized using the radius of the fibril, denoted by a. This value is set to $a = 1$ mm in all cases. The dimensionless height of the composite fibril is denoted by L/a, and its value is chosen as $L/a = 4$ in all investigated cases. This length has also been used in previous studies, as it is sufficiently large to ensure that the boundary condition applied to the top of the stack has no significant influence on the stress distribution at the bottom interface [7]. The dimensionless thickness of the soft tip is denoted by h/a, and values in the range $h/a = 0.05 \ldots 1$ are considered.

Two axisymmetric detachment modes are analyzed. Center detachment initiates from the axis of symmetry and propagates outward, while edge detachment starts at the outer edge of the contact interface and propagates inward. In both cases, the current dimensionless detachment length (measured from the initiation point) is denoted by c/a. The detachment process is covered from an initial detachment ($c/a = 0.004$) to almost complete detachment ($c/a = 0.996$) in increments of 0.004. (In selected cases, $c/a = 0.002 \ldots 0.998$ was considered with increments of 0.002.) The investigated parameters are summarized in Table 1.

The connection between the stiff stalk and the soft tip, as well as between the soft tip and the rigid substrate, is assumed to be perfectly bonded, except in the region where detachment has already occurred. The detachment process is modeled by gradually extending a traction-free zone along the contact interface, while the remaining part of the interface remains perfectly bonded. In this way, the model describes adhesive (interfacial) detachment rather than cohesive failure within the material. No explicit cohesive zone is introduced inside the solid; instead, the detachment is treated as a sharp interfacial crack, following the classical fracture mechanics approach (see, for example, [13]). Consequently, the stability analysis focuses on the energy release rate-based stability of the interfacial detachment and does not aim to represent cohesive material failure in the bulk. This simplification is appropriate for dry adhesive fibrils, where failure typically initiates at the contact interface rather than within the material itself.

We emphasize that this modeling approach does not introduce a new interface modeling technique but rather follows a well-established method commonly applied in similar studies.

The top interface is prescribed to move vertically by $\bar{u} = L/a/100$, while the bottom surface is fixed, creating a tensile load on the structure. Note that the actual value of $\bar{u}$ has no effect on the stability map calculations. The already detached region is assumed to have no interaction with the rigid plates and is therefore free of boundary conditions. In the FE software, the same mesh can be used for both detachment modes; only the boundary conditions along the bottom interface differ.

The numerical simulations were carried out using the finite element software Abaqus with an axisymmetric model. We employed CAX4H hybrid elements (or CAX4 elements when the Poisson's ratio was below 0.495) to model the structure. Because of the simple geometry, a structured mesh was easily generated. The mesh resolution was chosen such that the computed strain energy had a sufficiently low relative error compared to that of a denser mesh. Although the primary objective of this research is to determine stability, the mesh was also designed to allow for accurate stress evaluation. To achieve this, the element size was gradually reduced near the detachment front and along the contact interface, and additional refinement was applied at the interface between the two materials. This meshing strategy follows the approach described in our previous publication [15]. Furthermore, a detailed mesh-independence study was performed to verify the numerical accuracy of the results, and its outcomes are presented in Appendix.

Since a large number of simulations were required for this parametric study, model generation, meshing, evaluation, and data extraction (most importantly U) were fully automated using Python scripts.

Note that we investigate a displacement-driven case; thus, the potential energy (π) is equal to the stored strain energy in the system (U). Under displacement-controlled loading, this equivalence is a fundamental mechanical relationship, since no external work is done by varying forces. In practice, the total stored strain energy was obtained directly from the finite element simulations, as the Abaqus software automatically computes this quantity. The total value for the entire model was extracted from the "ALLSE" (total strain energy) output variable. It should be noted that in the present simulations, the "ALLSE" and "ALLIE" (internal energy) quantities are identical, because the model does not include nonlinear or dissipative energy contributions.

3.1. About stability calculation

Stability is determined according to Eq. (2). To apply this criterion, the value of U is obtained for several detachment lengths (c/a). The contact area (A) is then calculated based on the detachment length. In the case of edge detachment:

$$A = (a-c)^2\pi, \tag{3}$$

and for center detachment:

$$A = (a^2-c^2)\pi. \tag{4}$$

The meshing is controlled by the dimensionless parameter c/a, and the value of U is calculated for each mesh. From the relations above, the function $U(A)$ can be readily determined. The second derivative of $U(A)$ is required to assess stability. Since the function values are only available at discrete points, numerical differentiation is necessary. Several methods can be applied, but the specific choice has a negligible effect on the results. In this study, a spline of sufficiently high order was fitted to the data points and then differentiated twice. A Savitzky–Golay filter was applied to the second derivative to smooth the data, and the filtered result proved adequate for reliably evaluating stability.

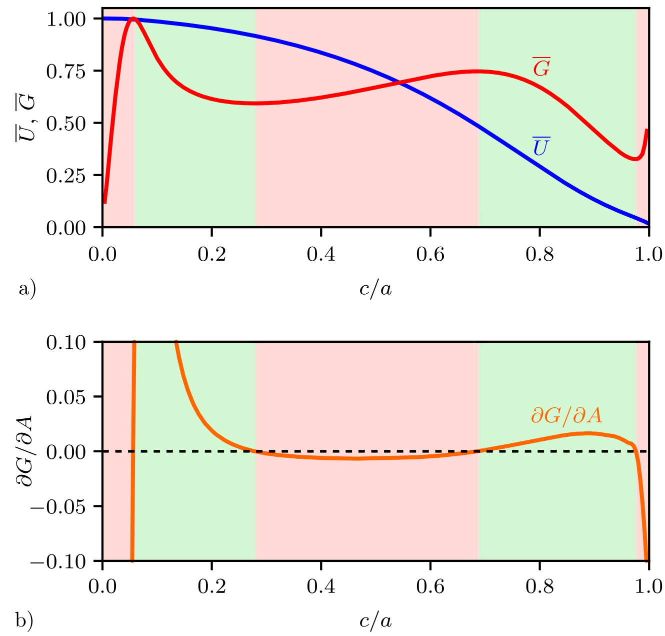

Fig. 3. Demonstration of the stability evaluation process for a selected center detachment case ($h/a = 0.1$, $\nu = 0.48$, $E_1/E_2 = 200$). (a) Normalized strain energy ($\overline{U}$) and normalized energy release rate ($\overline{G}$) plotted as a function of the dimensionless detachment length (c/a). (b) The derivative $\partial G/\partial A$ plotted against c/a, indicating detachment stability. Stable and unstable regions are highlighted with green and red background shading, respectively. (For interpretation of the references to color in this figure legend, the reader is referred to the web version of this article.)

The stability evaluation process is illustrated in Fig. 3, using data from a specific parameter combination (center detachment with $h/a = 0.1$, $\nu = 0.48$, $E_1/E_2 = 200$). Here, $\overline{U}$ and $\overline{G}$ denote the dimensionless normalized strain energy and the dimensionless energy release rate, respectively, calculated as

$$\overline{U} = \frac{U}{U_{max}} \quad \text{and} \quad \overline{G} = \frac{G}{G_{max}}, \tag{5}$$

where U_{max} and G_{max} denote the maximum values of U and G, respectively. The numerical values of $\overline{U}$, $\overline{G}$, and the derivative $\partial G/\partial A$ are plotted in Fig. 3. The red background indicates regions of unstable detachment, while the green background corresponds to stable detachment.

4. Results

As mentioned previously, the effects of three parameters are investigated: the Poisson's ratio (ν), the soft tip thickness (h/a), and the elastic modulus ratio (E_1/E_2). The values of these parameters are summarized in Table 1. In total, this parametric study involved 608,000 finite element simulations together with the corresponding numerical differentiation calculations.

Since the individual simulations are computationally inexpensive and demand limited resources, they were run in parallel on a single desktop PC. Still, the overall computational cost was rather significant. For a single parameter combination, the model generation using the Python script, the finite element solution, and the export of the results together took roughly one minute when using a single CPU core. The total computational time was approximately 608,000 min, equivalent to approximately 10,133 h or nearly 422 days of continuous computation: a substantial computational effort. However, by parallelizing the tasks on 16 separate threads, the total runtime was reduced to roughly 26 days. This total time does not include the post-processing of the simulation data, which also required additional effort.

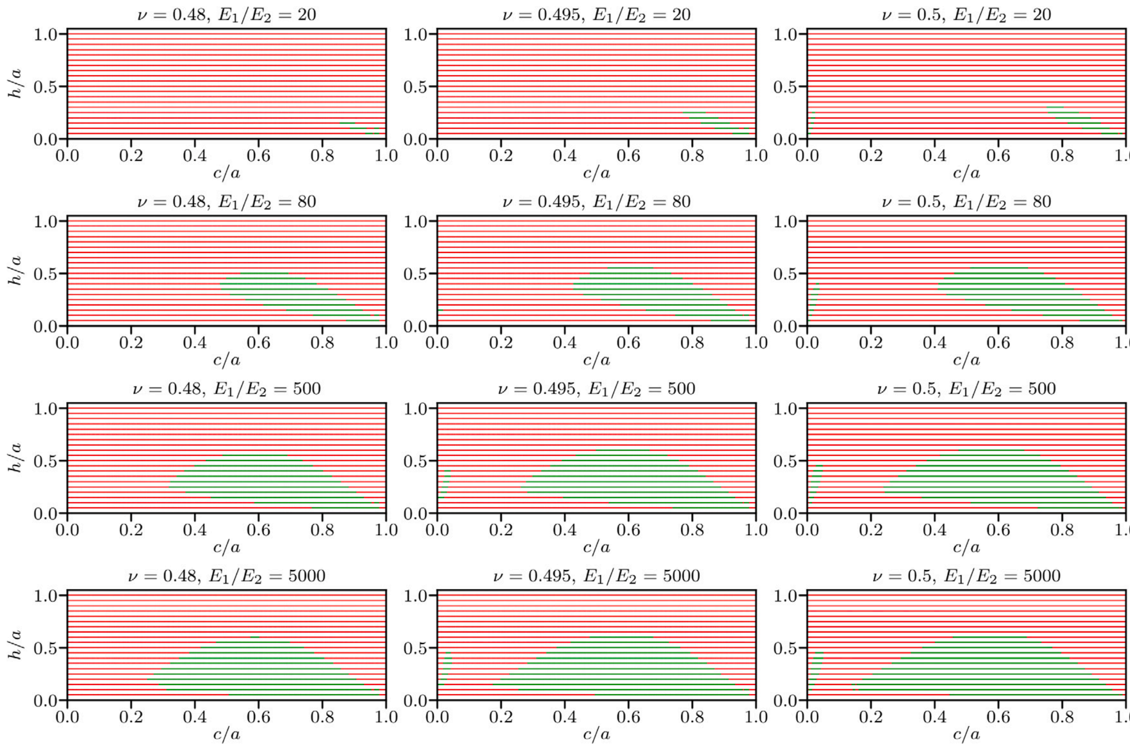

Fig. 4. Stability maps for the edge detachment case. The maps are arranged in a 4 × 3 grid according to modulus ratio (E_1/E_2) and Poisson's ratio (ν). Each row corresponds to a different modulus ratio (E_1/E_2 = 20, 80, 500, and 5000), while each column corresponds to a Poisson's ratio value (ν = 0.48, 0.495, and 0.5 from left to right). The maps show the stable (green) and unstable (red) regions as functions of the dimensionless detachment length (c/a) and soft layer thickness (h/a), providing a comprehensive overview of how detachment stability depends on material parameters in the edge detachment scenario. (For interpretation of the references to color in this figure legend, the reader is referred to the web version of this article.)

Selected stability maps obtained for the edge detachment case are presented in Fig. 4. These maps reveal several notable features of detachment stability. Detachment always starts and ends in an unstable manner. During the process, one or two continuous stable regions may exist. A narrow stability island appears at lower values of c/a, while a larger main stable region is observed at higher values of c/a. For each case, there exists a critical value of h/a, above which no stable region can be found. Decreasing the Poisson's ratio reduces the size of both stable domains. These trends are similar to those observed for the poker-chip problem [15].

However, significant differences emerge depending on the modulus ratio. Below $E_1/E_2 = 10$, no stable region exists. As the modulus ratio increases, the stable regions gradually expand. The effect of the modulus ratio on the shape of the main stable region differs from that of the Poisson's ratio. As E_1/E_2 increases, the main stable region first appears in the lower-right corner ($c/a \approx 1$, $h/a \approx 0.05$). It then takes on a droplet-like shape, and with further increase of E_1/E_2, it eventually extends toward smaller c/a values.

The stability island is absent when $E_1/E_2 \leq 10$, but it emerges at higher values. Its size — particularly its width — increases as the modulus ratio grows. Overall, these results show no qualitative differences compared to the trends observed with varying ν.

Similar stability maps were also created for the center detachment case, and selected results are presented in Fig. 5. Several characteristics are shared between the two detachment modes: detachment always starts and ends in an unstable manner, and one or two continuous stable portions may exist during the process. However, in the center detachment case, all stable segments are connected into a single continuous stable region. For each configuration, there exists a critical value of h/a, above which no stable region can be observed. Decreasing the Poisson's ratio reduces the size of the stable regions. These features are consistent with those found in the poker-chip problem as well as in the edge detachment case.

The modulus ratio also introduces significant differences. When $E_1/E_2 < 7$, no stable region exists. As the ratio increases beyond this threshold, the stable region first appears in the middle of the stability map, forming a narrow "bridge" that connects the center region to the lower-left corner ($c/a \approx 0$, $h/a \approx 0.05$). The stable zone takes on a droplet-like shape. As E_1/E_2 increases further, the stable zone expands toward smaller h/a values, particularly toward the lower-right corner ($c/a \approx 1$, $h/a \approx 0.05$). Interestingly, the shape of the stable region becomes concave for $10 \lesssim E_1/E_2 \lesssim 500$. This implies that, for a given h/a, a second stable section of comparable width may appear after the first one—most clearly visible in the case of $E_1/E_2 = 40$. Overall, the behavior governed by the modulus ratio differs considerably from that observed in the simpler poker-chip problem.

4.1. Analysis of critical thickness

The critical thickness (h_{cr}/a) represents the maximum thickness of the soft tip layer at which stable detachment can occur; such a value exists in all investigated cases. The value of h_{cr}/a is determined by interpolation: a spline is fitted through the boundary points of the stable region, and its maximum is identified. The specific interpolation method has only a minor effect on the results; here, cubic splines were used. Using the same approach, we also determine c_{cr}/a, which is the detachment length corresponding to h_{cr}/a. These results are presented in Fig. 6. (These quantities are shown only when a stable zone exists for a given E_1/E_2–ν combination.)

These metrics quantify the trends observed in the stability maps. In both the center and edge detachment cases, E_1/E_2 has a pronounced influence on both quantities, with the most significant changes occurring

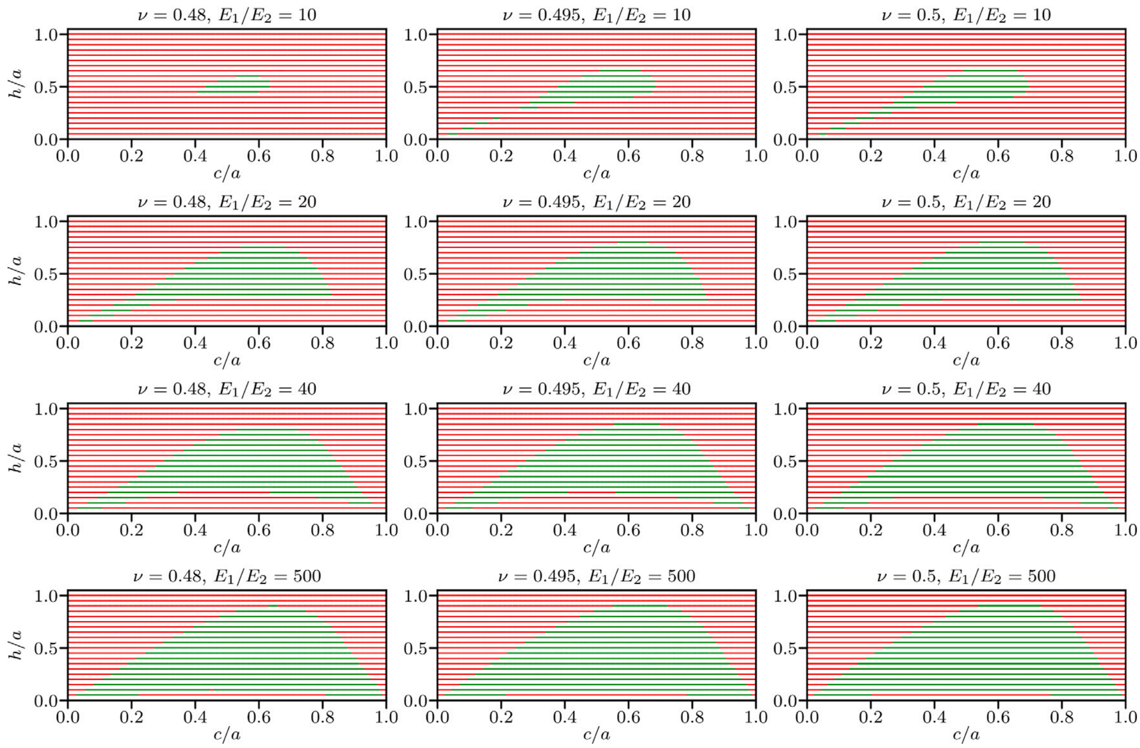

Fig. 5. Stability maps for the center detachment case. The maps are arranged in a 4 × 3 grid according to modulus ratio (E_1/E_2) and Poisson's ratio (ν). Each row corresponds to a different modulus ratio ($E_1/E_2 = 10$, 20, 40, and 500), while each column corresponds to a Poisson's ratio value ($\nu = 0.48$, 0.495, and 0.5 from left to right). The maps show the stable (green) and unstable (red) regions as functions of the dimensionless detachment length (c/a) and soft layer thickness (h/a), providing a comprehensive overview of how detachment stability depends on material parameters in the center detachment scenario. (For interpretation of the references to color in this figure legend, the reader is referred to the web version of this article.)

when $E_1/E_2 < 1000$. Higher values of either E_1/E_2 or ν correspond to higher h_{cr}/a. The variation of c_{cr}/a is also notable: in the center detachment case, the upper part of the stable zone shifts toward higher c/a values, while in the edge detachment case, the stable zone moves leftward on the maps, toward lower c/a values.

4.2. Size of the stable area

The shape of the stable zone is difficult to describe quantitatively. However, the overall size of the stable zone can be used to characterize the influence of the governing parameters. The stable area is calculated as the ratio of stable points to the total number of points in each map. In both detachment modes, the largest stable zone occurs when $\nu = 0.5$ and $E_1/E_2 = 1{,}000{,}000$. The results are presented in Fig. 7 as the relative stable area, normalized to the maximum stable area observed in each detachment case.

These results reveal several interesting features regarding the influence of the parameters. In both cases, the stable zone appears only above a certain value of E_1/E_2. For center detachment, stable zones emerge when $E_1/E_2 > 7$, while for edge detachment, they appear when $E_1/E_2 > 10$. This indicates the existence of a critical modulus ratio below which no stable region can form. Based on the parameter values used in our study, we can give a conservative estimate for this critical value, denoted as $E_{1,cr}/E_2$: approximately $E_{1,cr}/E_2 \approx 7$ for center detachment and $E_{1,cr}/E_2 \approx 10$ for edge detachment. Our methodology allows for refining these approximations by increasing the resolution of E_1/E_2 during the parameter sweep.

Increasing either ν or E_1/E_2 consistently enlarges the stable zone. As E_1/E_2 increases, the stable area grows faster in the case of center detachment. When $\nu = 0.5$, the relative stable area reaches about 80

The effect of increasing ν also differs slightly between the two cases. For $\nu = 0.48$, the relative stable area increases similarly in both modes, reaching about 80% only at $E_1/E_2 = 1{,}000{,}000$. However, for $\nu = 0.495$, the relative stable area becomes noticeably larger in the edge detachment case.

5. Additional discussion and remarks

Because all results were obtained using the same numerical framework, it is important to discuss the validation and possible limitations of the applied modeling approach. The following paragraphs summarize our considerations regarding experimental data, analytical solutions, and alternative numerical methods.

Comparing the numerical results with experimental data would strengthen the validation of the study. However, performing such experiments is extremely demanding, both technically and financially. The fabrication of suitable test specimens itself is complex and costly, and for common materials such as PDMS, setting the Poisson's ratio to a desired value is practically impossible. Furthermore, reproducing controlled center or edge detachments in a repeatable manner is particularly challenging. To our knowledge, no experimental data on the stability of detachment are currently available in the literature, most likely due to these challenges. Although our numerical results are not directly compared with experiments, we believe they provide valuable insight into the mechanics of the detachment process. The numerical framework allows us to generate arbitrary geometries, vary the elastic modulus ratio across a wide range, and set the Poisson's ratio freely. Furthermore, the finite element model enables the controlled initiation of both center and edge detachment scenarios. This methodology follows an approach commonly used in similar studies, focusing on the change in the stored strain energy as the key indicator of system stability.

Although the mechanical model might appear relatively simple, there is no available analytical solution for determining the effective

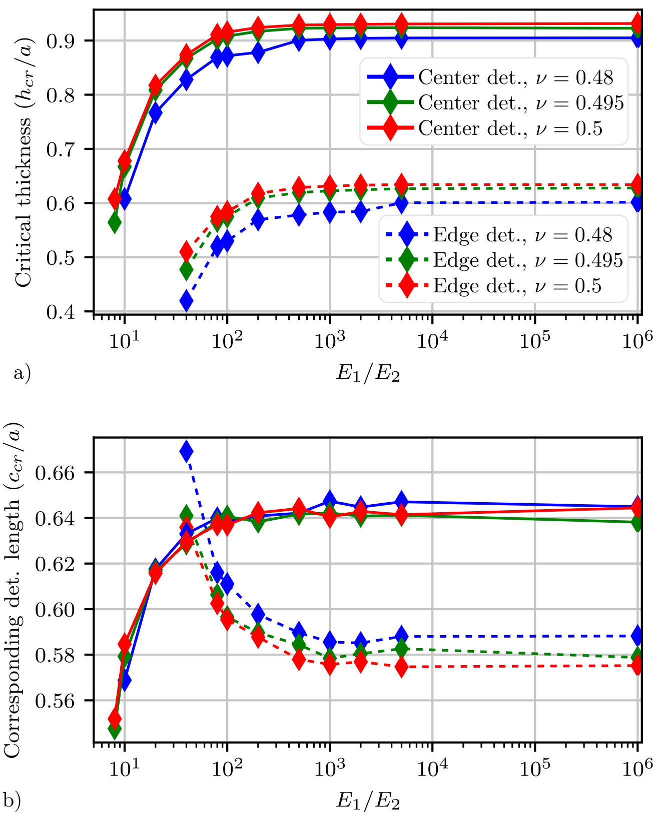

Fig. 6. Critical values characterizing the stability domain as a function of the modulus ratio (E_1/E_2) using a logarithmic horizontal axis. (a) Critical soft layer thickness h_{cr}/a and (b) the corresponding critical detachment length c_{cr}/a. Results are shown for three Poisson's ratio values: $\nu = 0.48$ (blue), $\nu = 0.495$ (green), and $\nu = 0.5$ (red). Solid lines represent center detachment cases, while dashed lines correspond to edge detachment. These plots quantify how the stability limit shifts with increasing stiffness contrast between the two layers. (For interpretation of the references to color in this figure legend, the reader is referred to the web version of this article.)

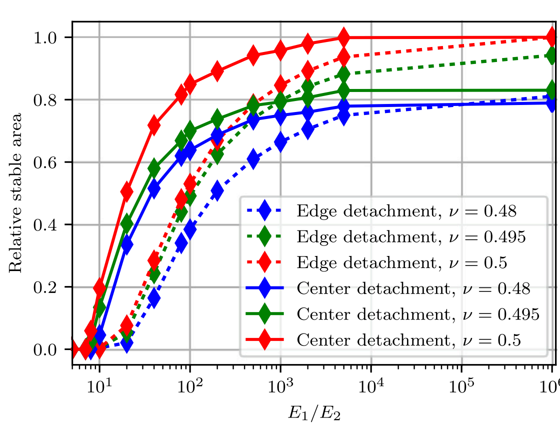

Fig. 7. Relative size of the stable area as a function of the modulus ratio (E_1/E_2), normalized by the maximal stable area obtained at $\nu = 0.5$ and $E_1/E_2 = 10^6$. A logarithmic scale is used on the horizontal axis. Results are shown for three Poisson's ratio values: $\nu = 0.48$ (blue), $\nu = 0.495$ (green), and $\nu = 0.5$ (red). Solid lines indicate center detachment cases, while dashed lines correspond to edge detachment. The plots reveal how the extent of the stable region increases with stiffness contrast and compressibility. (For interpretation of the references to color in this figure legend, the reader is referred to the web version of this article.)

axial stiffness or the stored strain energy in such a layered composite structure. The main difficulties arise from the boundary conditions along the contact interface and from the presence of materials with different elastic properties. Approximate analytical formulations could be derived with strong simplifications, but they would likely produce unreliable results with unknown errors. In our work, instead of applying such approximations, we directly solved the elasticity problem numerically for each parameter combination. The numerical reliability of the obtained results was ensured through detailed mesh-independence studies. While asymptotic stress solutions exist near the singularity zone, they cannot be used to calculate the total strain energy for arbitrary geometries or detachment sizes. Therefore, no meaningful analytical comparison is possible, and a simplified formula would not improve the understanding of the phenomenon.

The energy release rate (G) can also be calculated using contour-integral methods such as the J-integral. In a previous study on the slightly compressible poker chip detachment problem [15], we verified that the G values obtained using J-integrals and those derived from direct differentiation of the strain energy are numerically identical. This earlier work confirmed the reliability of the simpler approach used in the present study. For completeness, we also verified a few selected cases of the composite fibril model using the J-integral method and again found identical numerical results. These additional checks support the consistency of our approach. As no other practical methods are available for determining the energy release rate in this type of problem, we consider our modeling framework both robust and validated within its intended scope.

Although the present study focuses on quasi-static detachment, viscoelastic effects may become important when dynamic or rate-dependent adhesion processes are involved. The finite element framework applied here can be extended to incorporate viscoelastic material models if required. In fact, several recent works have demonstrated that including time-dependent material behavior can significantly affect the predicted pull-off force, hysteresis, and energy dissipation during detachment. Such viscoelastic modeling approaches have already been applied to study adhesion in bio-inspired mushroom-shaped fibrillar structures [23,24]. While this effect is beyond the scope of the current quasi-static analysis, these studies highlight how viscoelasticity can play a crucial role in dynamic adhesion and should be considered in future investigations of similar systems.

6. Conclusion

In this work, we investigate the detachment of a bi-material composite fibril from a rigid substrate. The effects of three governing parameters are analyzed: the dimensionless thickness of the bottom layer (h/a), the Poisson's ratio (ν), and the modulus ratio between the stalk and the soft tip (E_1/E_2). Stability maps are presented for the studied cases, revealing several important characteristics. The main findings can be summarized as follows:

- In all cases, there exists a critical value of h/a, above which detachment becomes entirely unstable.
- Decreasing the Poisson's ratio noticeably reduces the size of the stable area, although the overall shape of the stable domain remains nearly unchanged.
- The modulus ratio has a pronounced effect on both the size and shape of the stable zone. Detachment can occur in a stable manner only if the modulus ratio is sufficiently high. Based on our conservative estimates, for edge detachment $E_1/E_2 > 10$ and for center detachment $E_1/E_2 > 7$ must be satisfied for stable propagation to occur. Further increasing this ratio significantly enlarges the stable domain.
- These results are consistent with expectations from previous studies in the limiting cases. Specifically, when $E_1/E_2 = 1$, no stable zone exists, while at $E_1/E_2 = 1{,}000{,}000$, the size and shape of the stable zone correspond well with those of the poker-chip problem.

- Increasing either the Poisson's ratio or the modulus ratio always enlarges the stable zone. If a given parameter combination leads to stable detachment, stability will persist for all higher values of ν or E_1/E_2. Therefore, to maximize the size of the stable domain, one should select nearly incompressible materials combined with a high modulus ratio.

Our methodology can be readily applied to materials with different Poisson's ratios. In this study, the Poisson's ratio was found to have a considerably smaller influence on stability properties than the modulus ratio. Nevertheless, its effect is still noticeable; therefore, a more detailed investigation of varying Poisson's ratios should be the focus of future research.

The results presented here were obtained using an idealized model. In real systems, detachment may exhibit more complex behavior. However, our findings clearly indicate that the modulus ratio plays a crucial role in determining stability and should be taken into account when analyzing real-world detachment phenomena. The modulus ratio between the substrate and the elastic material is also expected to influence experimental measurements.

CRediT authorship contribution statement

András Levente Horváth: Writing – review & editing, Writing – original draft, Visualization, Validation, Software, Resources, Project administration, Methodology, Investigation, Funding acquisition, Formal analysis, Data curation, Conceptualization. **Attila Kossa:** Writing – review & editing, Writing – original draft, Visualization, Validation, Supervision, Software, Resources, Project administration, Methodology, Investigation, Funding acquisition, Formal analysis, Data curation, Conceptualization.

Declaration of competing interest

The authors declare that they have no known competing financial interests or personal relationships that could have appeared to influence the work reported in this paper.

Acknowledgments

This research was supported by the Hungarian National Research, Development and Innovation Office (FK 142457). This research was supported by the János Bolyai Research Scholarship of the Hungarian Academy of Sciences.

Appendix. Mesh layout and convergence verification

Mesh layout diagram. For the finite element discretization, we used four-node quadrilateral elements in all cases. In every simulation, only regular rectangular elements were applied, as they are numerically more stable. The mesh was refined in those regions of the structure where the stress field changes more significantly. The most important of these regions is the area located just ahead of the detachment front.

Developing the meshing strategy required quite a lot of work, but with this effort we managed to create a mesh layout that gave results we could consider converged for the studied phenomenon. It is also important to note that the meshing process itself was performed using a Python script. To make the Python script simpler to define, we applied radial mesh refinement along the full vertical length of the fibril above the detachment front. Although such refinement is not strictly needed far from the soft tip, it made the scripting much easier, and the denser mesh did not significantly increase the computation time.

The structure of the applied mesh layout is shown through one selected sample case, since the same layout was used for all other simulations as well, with the only difference being that the element sizes change depending on the soft tip layer thickness and the detachment length. The mesh structure is not affected by the ratio of the elastic moduli or by the value of the Poisson's ratio.

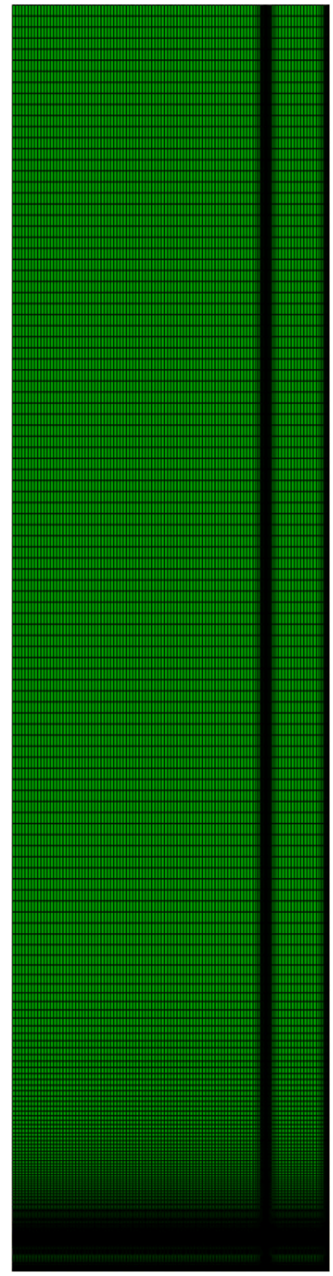

Fig. A.8. Finite element mesh used for the simulation in the case of $h/a = 0.1$ and $c/a = 0.2$, for the edge detachment scenario.

Fig. A.8 shows the finite element mesh for the case of $h/a = 0.1$ and $c/a = 0.2$ in the edge detachment configuration. The image resolution does not allow a detailed display of the individual elements in the highly refined regions; therefore, the element boundary lines merge together, and these areas appear as solid black zones.

Fig. A.9 presents only the mesh of the soft tip layer across the full text width. In this enlarged view the element sizes and their distribution can be clearly seen. In this sample case, a total of 27,951 elements were used, which define 28,304 nodes. Within the soft tip layer, there are 5490 elements in total.

Mesh convergence verification. Before selecting the final mesh used for the analysis, we performed a detailed convergence study with respect to the element size. We could rely on the results of our previous

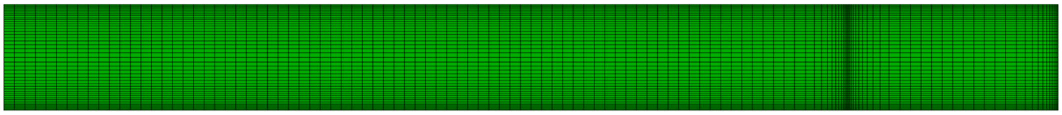

Fig. A.9. Finite element mesh used for the simulation in the case of $h/a = 0.1$ and $c/a = 0.2$, for the edge detachment scenario. In the figure, only the soft tip layer is shown, while the mesh of the upper, stiffer stalk is not displayed.

Table A.2
Data of the meshes used for the convergence study.

ID	Global seed size	Elements	Nodes
Mesh-1	0.1	400	451
Mesh-2	0.05	1600	1701
Mesh-3	0.025	6400	6601
Mesh-4	0.0125	25,600	26,001
Mesh-5	0.006	110,722	111,556
Mesh-6	0.003	445,222	446,890
Mesh-7	0.0015	1,776,222	1,779,556
Mesh-8	0.0008	6,250,000	6,256,251
Mesh-9	0.0004	25,000,000	25,012,501

publication on a similar topic, as well as on mesh-independence studies reported by others, but we still carried out a full convergence check for the present problem as well.

The effect of element size on the results is shown here through one representative case among many. The selected example corresponds to the same configuration described earlier in the mesh layout section: edge detachment case, $h/a = 0.1$, $c/a = 0.2$, $E_1/E_2 = 200$, $\nu = 0.48$. For this problem, we created nine different finite element meshes, where the global element size was systematically reduced by a factor of two (or approximately two in some cases).

In Abaqus, the *Global Seed Size* parameter was used for this refinement, which helps the software generate mostly regular, nearly square-shaped elements. The properties of the applied finite element meshes are summarized in Table A.2. In the finest mesh (Mesh-9), the model consists of 25 million elements, out of which 625,000 elements belong to the soft tip layer.

The meshes listed in Table A.2 are shown in Fig. A.10. The cases Mesh-7, Mesh-8, and Mesh-9 are not displayed because, similar to the Mesh-6 case, the element size cannot be clearly seen due to the image resolution. To illustrate the three finest meshes, we show only the mesh within the soft tip layer in Fig. A.11. Even in this enlarged view, the individual elements of the finest mesh are not visible; however, the overall meshing strategy can still be clearly understood from the figures.

In the phenomenon studied in our manuscript, the main quantity of interest is the strain energy stored in the system, since our stability maps are derived directly from this energy. For the meshing strategies listed in Table A.2, the obtained strain energy values are plotted in Fig. A.12 as a function of the total number of elements, shown in blue. Fig. A.12b presents the results using logarithmic scales for the axes. The Mesh-1 … Mesh-9 cases are marked in blue, while the red line indicates the result obtained with our own meshing method.

By visual inspection, we can observe that the result obtained with our mesh (red line) shows perfect agreement with the value from the finest mesh (Mesh-9). Moreover, no further change in the strain energy is observed when the element size is reduced, therefore the Mesh-9 result can be considered a numerically converged reference solution.

The strain energy value obtained with the Mesh-9 mesh is 35.7972, while our designed mesh gives 35.8078, resulting in a relative difference of 0.0002961. It is also worth noting that the relative difference between the results of Mesh-8 and Mesh-9 is only 0.0001089. Based on these observations, we concluded that the solution obtained with our mesh is accurate and reliable for the investigated phenomenon.

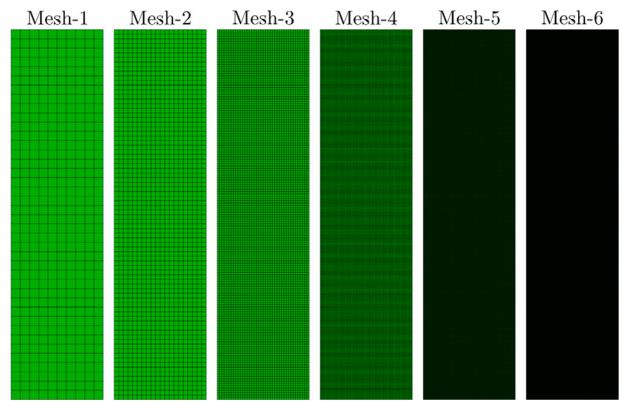

Fig. A.10. Images of the meshes corresponding to the Mesh-1 … Mesh-6 meshing strategies. The Mesh-7, Mesh-8, and Mesh-9 cases are not shown, because, similar to Mesh-6, the element size cannot be distinguished due to the image resolution.

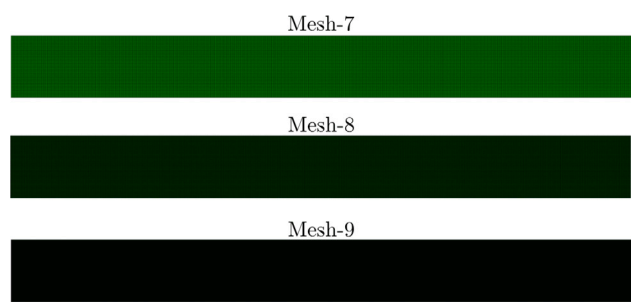

Fig. A.11. Meshes corresponding to the Mesh-7, Mesh-8, and Mesh-9 meshing strategies shown for the soft tip layer.

Although the paper does not focus on the stress distribution along the contact interface, during the mesh convergence study we also examined how the normal stress varies along the interface depending on the applied mesh. The corresponding results confirmed that the stress distributions are also convergent and consistent with the energy-based conclusions; however, those figures are not included here for brevity.

Based on the detailed convergence study described above, we can state that the results obtained with our mesh are numerically reliable and suitable for analyzing the mechanical phenomenon investigated in the manuscript.

Data availability

Data will be made available on request.

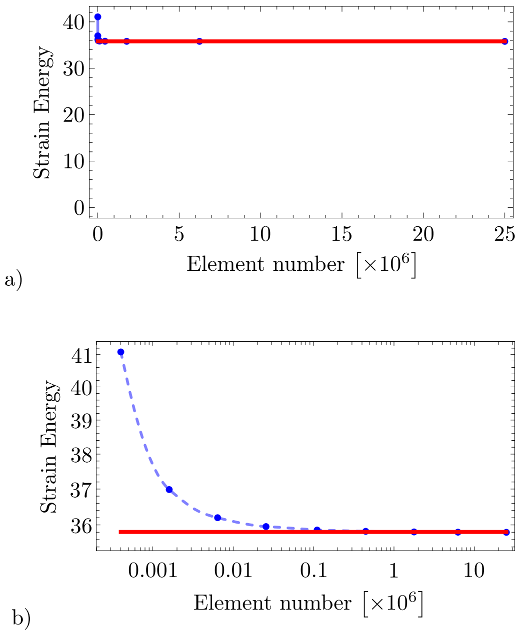

Fig. A.12. Change of the strain energy as a function of the total number of elements. The Mesh-1 … Mesh-9 cases are shown in blue, while the red line indicates the result obtained with our own meshing method. (For interpretation of the references to color in this figure legend, the reader is referred to the web version of this article.)

References

[1] C.S.P. Borges, A. Akhavan-Safar, P. Tsokanas, R.J.C. Carbas, E.A.S. Marques, L.F.M. da Silva, From fundamental concepts to recent developments in the adhesive bonding technology: a general view, Discov. Mech. Eng. 2 (1) (2023) 8, http://dx.doi.org/10.1007/s44245-023-00014-7.

[2] R.D. Adams, Adhesive Bonding: Science, Technology and Applications, second ed., in: Woodhead Publishing Series in Welding and Other Joining Technologies, Woodhead Publishing, 2021.

[3] M.P. Murphy, S. Kim, M. Sitti, Enhanced Adhesion by gecko-inspired hierarchical fibrillar adhesives, ACS Appl. Mater. Interfaces 1 (4) (2009) 849–855, http://dx.doi.org/10.1021/am8002439.

[4] X. Li, P. Bai, X. Li, L. Li, Y. Li, H. Lu, L. Ma, Y. Meng, Y. Tian, Robust scalable reversible strong Adhesion by gecko-inspired composite design, Friction 10 (8) (2022) 1192–1207, http://dx.doi.org/10.1007/s40544-021-0522-4.

[5] R. Balijepalli, M. Begley, N. Fleck, R. McMeeking, E. Arzt, Numerical simulation of the edge stress singularity and the Adhesion strength for compliant mushroom fibrils adhered to rigid substrates, Int. J. Solids Struct. 85–86 (2016) 160–171, http://dx.doi.org/10.1016/j.ijsolstr.2016.02.018.

[6] R.G. Balijepalli, S.C. Fischer, R. Hensel, R.M. McMeeking, E. Arzt, Numerical study of Adhesion enhancement by composite fibrils with soft tip layers, J. Mech. Phys. Solids 99 (2017) 357–378, http://dx.doi.org/10.1016/j.jmps.2016.11.017.

[7] A. Kossa, R. Hensel, R.M. McMeeking, Adhesion of a cylindrical punch with elastic properties that vary radially, Mech. Res. Commun. 130 (2023) 104123, http://dx.doi.org/10.1016/j.mechrescom.2023.104123.

[8] S.-W. Chen, G.-F. Wang, M. Ciavarella, Optimal grading of elastic modulus at contact corners with friction with application in fibrillar adhesives, Eur. J. Mech. A Solids 113 (2025) 105673, http://dx.doi.org/10.1016/j.euromechsol.2025.105673.

[9] G. Carbone, E. Pierro, S.N. Gorb, Origin of the superior adhesive performance of mushroom-shaped microstructured surfaces, Soft Matter 7 (2011) 5545–5552, http://dx.doi.org/10.1039/C0SM01482F.

[10] G. Violano, S. Dibitonto, L. Afferrante, Adhesive contact mechanics of bio-inspired pillars: Exploring hysteresis and detachment modes, Int. J. Adhes. Adhes. 134 (2024) 103768, http://dx.doi.org/10.1016/j.ijadhadh.2024.103768.

[11] D. Li, Y. Yan, R. Li, Q. Gao, C. Xu, W. Zhang, Insight into the dynamic Adhesion of bio-inspired mushroom-shaped micropillars, Tribol. Int. 214 (2026) 111274, http://dx.doi.org/10.1016/j.triboint.2025.111274.

[12] Y. Li, B. Sun, M. Li, H. Tian, J. Xu, H. Hou, Z. Zhang, D. Gao, W. Li, H. Yan, X. Ning, J. Shao, Mushroom-shaped adhesive structures with smooth contour via electrical growth, ACS Appl. Mater. Interfaces 17 (20) (2025) 30170–30180, http://dx.doi.org/10.1021/acsami.4c21993.

[13] R.E. Webber, K.R. Shull, A. Roos, C. Creton, Effects of geometric confinement on the adhesive debonding of soft elastic solids, Phys. Rev. E 68 (2003) 021805, http://dx.doi.org/10.1103/PhysRevE.68.021805.

[14] R.M.M. René Hensel, A. Kossa, Adhesion of a rigid punch to a confined elastic layer revisited, J. Adhes. 95 (1) (2019) 44–63, http://dx.doi.org/10.1080/00218464.2017.1381603.

[15] A.L. Horváth, A. Kossa, Stability maps for the slightly compressible poker chip detachment problem, Finite Elem. Anal. Des. 242 (2024) 104257, http://dx.doi.org/10.1016/j.finel.2024.104257.

[16] A. Kumar, O. Lopez-Pamies, The poker-chip experiments of Gent and Lindley (1959) explained, J. Mech. Phys. Solids 150 (2021) 104359, http://dx.doi.org/10.1016/j.jmps.2021.104359.

[17] F.V. Antunes, J.M. Ferreira, J. Byrne, Stress intensity factor calculation based on the work of external forces, Int. J. Fract. 98 (1) (1999) 1–14, http://dx.doi.org/10.1023/A:1018684932071.

[18] H. Millwater, D. Wagner, A. Baines, A. Montoya, A virtual crack extension method to compute energy release rates using a complex variable finite element method, Eng. Fract. Mech. 162 (2016) 95–111, http://dx.doi.org/10.1016/j.engfracmech.2016.04.002.

[19] A.A. Griffith, G.I. Taylor, VI. The phenomena of rupture and flow in solids, Philos. Trans. R. Soc. Lond. Ser. A, Contain. Pap. A Math. Or Phys. Character 221 (582–593) (1921) 163–198, http://dx.doi.org/10.1098/rsta.1921.0006.

[20] A.L. Horváth, A. Kossa, 3D stability analysis of the poker chip detachment problem, J. Theoret. Appl. Mech. (2025) http://dx.doi.org/10.15632/jtam-pl/202927.

[21] S. Khaderi, N. Fleck, E. Arzt, R. McMeeking, Detachment of an adhered micropillar from a dissimilar substrate, J. Mech. Phys. Solids 75 (2015) 159–183, http://dx.doi.org/10.1016/j.jmps.2014.11.004.

[22] M. Samri, A. Kossa, R. Hensel, Effect of subsurface microstructures on Adhesion of highly confined elastic films, J. Appl. Mech. 88 (3) (2020) 031009.

[23] G. Violano, S. Dibitonto, L. Afferrante, Role of viscoelasticity in the Adhesion of mushroom-shaped pillars, Bioinspir Biomim (2024).

[24] R.-G. Ji, Y.-Y. Yuan, X.-F. Liu, X.-L. Zhang, G.-P. Cai, Modeling the pull-off force of a mushroom-shaped fibrillar adhesive in dynamic detachment, Int. J. Solids Struct. 308 (2025) 113150, http://dx.doi.org/10.1016/j.ijsolstr.2024.113150.